UAS-Based Radio Frequency Interference Localization using Power Measurements

Casey Smith, Haoming Yan, Osama Abdul Hafez, Jeremy Hopwood, Mathieu Joerger, *Virginia Tech*

BIOGRAPHIES

Casey Smith is a master's student in Aerospace Engineering and a graduate research assistant in the Assured Vehicle Autonomy Lab (AVA) at Virginia Tech. He obtained his BS in Mechanical Engineering in 2019 from Rowan University, NJ. His specialization is in dynamics, controls, and estimation with research focused on GNSS jamming.

Haoming Yan is a master's student in Aerospace Engineering at Virginia Tech working with Dr. Mathieu Joerger. He is also a graduate research assistant in the Assured Vehicle Autonomy Lab (AVA) at Virginia Tech. He obtained a BS in aerospace engineering in 2022 from the University of Arizona, Tucson. His interests are in the fields of dynamics and control of Un-crewed Aircraft Systems (UAS) and GNSS jammer localization.

Osama Abdul Hafez is a postdoctoral researcher at Virginia Tech. He obtained his MEng(2020) and PhD(2023) in Mechanical and Aerospace Engineering and MS(2021) in Autonomous Systems and Robotics from Illinois Institute of Technology. His research involves localization and control techniques applied to autonomous vehicle navigation problems with an emphasis on GNSS and Non-GNSS localization and control safety methods.

Jeremy Hopwood is a Ph.D. candidate in the Aerospace and Ocean Engineering department at Virginia Tech. In the Non-linear Systems Laboratory under his advisor Craig Woolsey, his research involves non-linear estimation and control of aircraft in stochastic environments using passivity-based and robust control techniques with flight test validation.

Dr. Mathieu Joerger is an assistant professor at Virginia Tech. He obtained a Master's in Mechatronics from INSA Strasbourg, France (2002) and MS (2002) and PhD (2009) in Aerospace Engineering from the Illinois Institute of Technology, Chicago. He received the ION Bradford Parkinson Award in 2009, the ION Early Achievement Award in 2014, the ION Burka Award and Thurlow Award in 2023. He is the senior editor on navigation of IEEE Transactions on Aerospace and Electronic Systems.

ABSTRACT

This paper describes the development, implementation, and testing of a GNSS jammer localizer using power measurement profiles collected during un-crewed aerial system (UAS) fly-bys. A linearized measurement equation based on the Friis power transmission formula is derived in which RF channel propagation parameters are grouped into a single parameter for estimation. Synchronized power and UAS position measurements are processed in a batch-type sequential non-linear least squares algorithm for simultaneous estimation of static jammer position and received power model parameters. We develop a low size, weight, power, and cost (SWAP-C) quad-rotor UAS test bed that can collect and time-stamp power measurements with UAS position. Since GNSS jamming is illegal, a LoRa 868 MHz transmitter is used as a surrogate GNSS jammer during field testing – providing Received Signal Strength Indicator (RSSI) measurements to the LoRa receiver onboard the UAS. Testing is conducted at the Virginia Tech Kentland Experimental Aerial Systems Lab, where emitter localization is evaluated for three different trajectories. Experimental performance analysis suggests that meter-level localization accuracy is achievable with prior knowledge on source location and by accounting for antenna gain pattern variations over time in the estimation process with a first order Gauss Markov Process.

1 INTRODUCTION

In this paper, we develop, implement, and test a sequential, non-linear estimation method aimed at localizing a single, static RF emitting source using received power measurements. The prototype hardware is designed for field testing of RF interference (RFI) localization using a LoRa (868 MHz) protocol device as a surrogate for illegal GNSS jamming. The algorithm is implemented on an un-crewed aerial system (UAS) carrying a low-cost LoRa receiver. Signal power variations during UAS fly-bys are used to localize the signal source. Testing performed using a quad-rotor shows that transmit power and emitting antenna gain variations must be estimated simultaneously with source position to achieve meter-level localization.

Military conflict regions around the world have experienced an increase in wide-area radio frequency interference (RFI), including in Syria since 2018 (Liu, 2020), near the Russia – Ukraine border in 2020 and 2021 (Goward, 2021; Jones, 2020), and with increased intensity and spread in the Eastern Mediterranean Sea since October 2023 (Murfin, 2023). Such high-power jammers are observable at far-away locations and have been successfully localized using Low Earth Orbit (LEO)-based receivers.

Civilian applications are subject to RFI as well. Wide-area GNSS interference events, including the one near the Dallas–Fort Worth airport on October 17 and 18, 2022 have been investigated but their source has yet to be identified (Joerger et al., 2023). Low power RFI from low-cost commercially-available GNSS jammers, including personal privacy devices (PPDs), are widespread but only locally observable (Pul1en & Gao, 2012). PPDs used by motorists have caused GNSS service disruptions at major airports and along busy aviation corridors (Jada, 2022).

The increase in RFI events motivates the development of RFI source detection and localization strategies. Since these devices are concealable and commercially proliferating, a lightweight, cost effective, and swiftly deployable system is required. Authorities wishing to mitigate jamming require warrants to search vehicles. They therefore need high-confidence jammer position estimates, with meter-level accuracy to single-out a vehicle in a parking lot of a port or warehouse. The estimator and test bed in this work assumes that localization takes place at one of these facilities, where ground detectors like those discussed below can provide an initial guess on RFI source position.

Prior work on GNSS jamming detection includes monitoring of carrier to noise ratio (C/N0) (Borio & Gioia, 2015), relative received power at GPS L1 frequency band (Jada et al., 2021, 2022, 2023), and direction of arrival (Marcos et al., 2018). These methods provide detection but do not enable source localization.

Fixed antenna systems can be locally effective for localization, but they may not be widely scalable. The RFI monitors presented in (Bauernfeind & Eissfeller, 2014; Šture et al., 2019) only monitor a limited region – and require multiple stations to perform localization. An earlier implementation, the generalized interference detection and localization system (GIDL), demonstrated sub-meter accuracy when receiver geometry is favorable (Gromov et al., 2000). In general, fixed antennas may not provide sufficient accuracy but could direct the deployment of more local RFI localization systems – such as fixed-wing or multi-rotor drone-based solutions.

Un-crewed Aerial Systems (UASs) offer a platform to precisely search a local region. Localization can be performed since a UAS-based receiver makes observations from multiple locations. Regarding UAS localization, prior experimental work in the presence of live jamming shows that UAS GPS-based positioning is possible if the UAS stays far enough from the source to avoid being jammed, but close enough to observe power variations at GPS frequencies. While remaining at a safe distance from a jammer, observed power variations were an order of magnitude larger than nominal power without the positioning accuracy of a standard GPS receiver (located at the monitor's location) being altered (Jada et al., 2022).

UAS deployment requires little infrastructure and enables line-of-sight collection of RFI signals that would be occluded at ground-based receivers. Prior work on UAS-based RF source localization includes using angle of arrival, which requires calibrated directional antennas (large size, weight, power, and cost (SWAP-C)) and constrained UAS rotation (Perkins et al., 2016; Wu, 2018). Multi-UAS collaborative approaches can eliminate the need for angle of arrival measurements (Bhamidipati & Gao, 2018, 2019; Güzey, 2022; Liu et al., 2022) but may not be as cost-effective or scalable as single UAS strategies.

Real-time reinforcement learning and particle filtering approaches have been proposed for deployment on single UAS systems (Hasanzade et al., 2018; Wu, 2018). These are computationally expensive algorithms – resulting in high SWAP-C platforms. This is addressed by Kwon and Guvenc (2023) by using linear least squares (LLS) localization algorithms. However, they implement a large matrix of predefined trajectory waypoints that require long flight durations for wide area coverage - something that could prove challenging for a low cost or small footprint UAS system.

In this paper, we develop a non-linear least squares (NLS) localization algorithm with a-priori state knowledge that leverages range variations over multiple UAS fly-bys to localize the RFI source. Range variations are derived from power measurements modeled using the Friis power transmission formula. Unknown source antenna gain variations over line-of-sight changes during UAS flyby are modeled as a time-correlated random process. We also design a UAS-based RFI source localization test bed using low SWAP-C components. The regulations on transmitting at GPS L1 make data collection and field testing of GPS jamming challenging. Instead, we use the LoRa ("long range") communication protocol as a surrogate RFI signal to collect relative power measurements at the 868 MHz frequency.

The remainder of this paper is organized as follows. In Section 3, we derive the power measurement error model and its incorporation in a NLS localization algorithm. Section 4 outlines the test bed architecture. Section 5 presents experimental results. Concluding remarks are given in Section 6.

2 BACKGROUND AND JAMMER LOCALIZATION PRINCIPLE

2.1 Background and Motivation: Field Observations

In prior work (Jada et al., 2021, 2022), we processed months of GNSS carrier to noise ratio (C/N0) data from Continuously Operating Reference Stations (CORS) and from the International GNSS Service (IGS). We implemented the high-sensitivity, self-calibrating C/N0 monitors developed in (Jada et al., 2021) to detect drops in C/N0 simultaneously occurring on all GPS L1 satellite signals, which are a strong indication of jamming.

An example result of this research is shown in Figures 1(a)-(b) for C/N0 monitoring near the Schriever Air Force Base in Colorado Springs, Colorado during the months of January to August 2022. Figure 1(a) shows detected events on a day-of-year (y-axis) versus time-of-day (x-axis). The color-code from blue to red represents days of the week, from Monday to Sunday. The marker size shows the intensity of the detected event as measured by the test statistic described in (Jada et al., 2022). The window insert shows an example event where the GPS L1 C/N0 drops for all 10 satellite signals visible at that time and location. The C/N0 then quickly rises again to its nominal value indicating that the vehicle carrying the jammer quickly approached and left the location. Figure 1(b) is a histogram of the number of detection occurrences versus day of week. Figures 1(a)-(b) suggests that the user of a jammer is regularly driving to and from a daily activity (probably work) every weekday at 6:00AM and 2:00PM, respectively.

This regular pattern makes jamming at that location predictable. We deployed our own dedicated equipment, including an RF front-end receiver (a Universal Software Receiver Peripheral, or USRP) and collected power data at that location. The resulting measurements, in uncalibrated RF front-end units, are shown in Figure 1(c). This is "live" jamming data from a fast-moving jammer collected at a slowly moving location driving in the opposite direction. Figure 1(c) shows an increase in received power, reaching up to ten times the nominal power level followed by a decrease in received power. A sudden dip in received power at time 219 s was probably caused by line-of-sight occlusion from another vehicle driving between emitter and receiver.

Many such power profiles were observed during our data collection campaigns both at static and moving receivers. In parallel, we collected data from a commercial u-blox M8 receiver to perform sanity checks. In most cases, including in the case of Figure 1(c), the u-blox receiver seemed unaffected by the interference: the u-blox receiver kept track of its position and did not exhibit significant C/N0 variations during the event. This suggests that if the power monitor is sensitive enough, RFI sources can be detected and localized while maintaining GNSS service for use by the UAS. After spectrogram analysis, we determined that the jammer in Figure 1(c) was a personal privacy device (PPD). This supports the use of a UAS in the presence of these style of jammers, as GPS can be used to determine the position of a (moving) jammer-localizer (such as a UAS) as long as the jammer-localizer stays far enough from the RFI source.

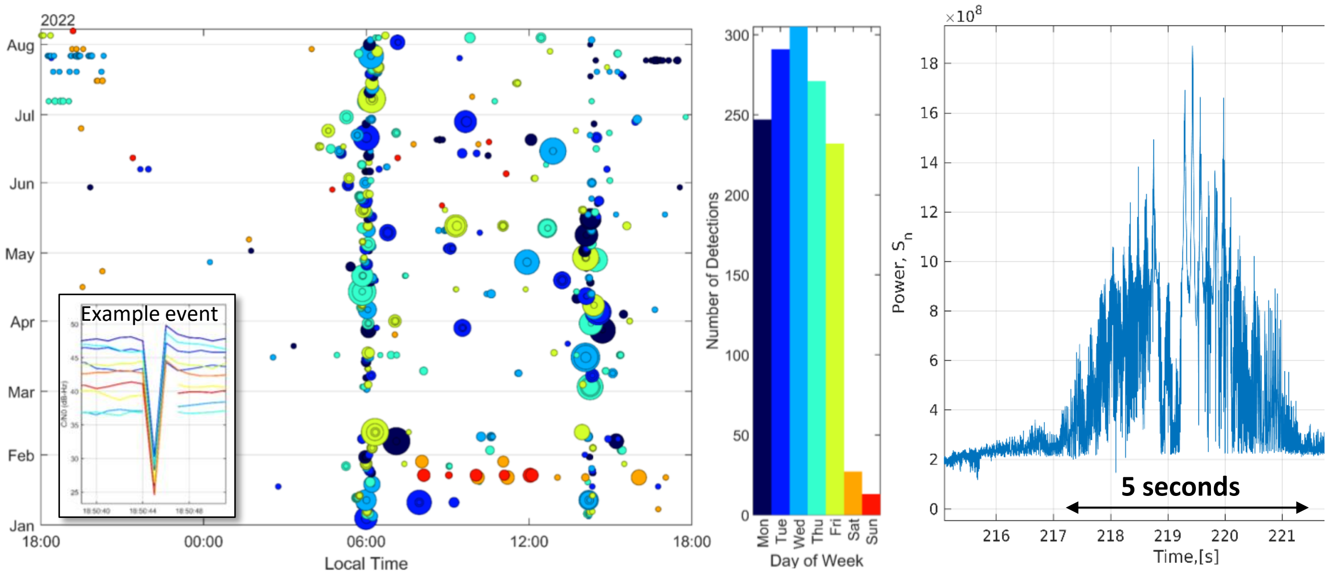

(a) **(b)** **(c)**

FIGURE 1 Relevant prior research in (Jada et al., 2022) **(a)** C/N0-based detection events, **(b)** Number of detected events per day of week, **(c)** Power profile of a car-based jammer observed at a static receiver.

2.2 Jammer Localization Principle

This paper addresses the use case of a jammer entering a facility that needs to be protected against RFI, such as an automated port, airport, or delivery warehouse. Figure 2 illustrates a conceptual overview of the system. We assume that fixed ground monitors at the facility's entry points, or other wide-area monitors like those mentioned in Section 1, are able to detect jammers. Such detection triggers the deployment of one or more UAS. The UAS uses the ground monitor's indication as rough prior knowledge of the jammer's location. It flies to that approximate location with the objective of localizing the source of emission with meter-level accuracy. This position estimate must be accurate enough to identify the jammer-carrying vehicle. This estimate can then be used as evidence by competent authorities at the Federal Communications Commission (FCC) to perform a search of the designated vehicle.

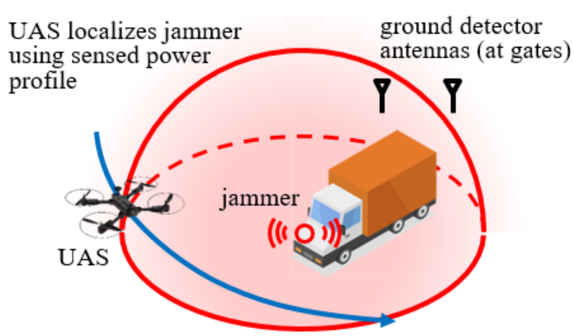

FIGURE 2 Overview of the jammer localization concept.

3 POWER-BASED JAMMER LOCALIZATION ALGORITHM DERIVATION

A UAS flying by an RFI source experiences a peak in received power at the UAS-to-jammer closest point of approach (CPA), as long as the UAS maintains an un-obstructed line-of-sight (LOS) to the jammer. If the emitting and receiving antennas have isotropic gain patterns, the received power should ramp-up and ramp-down as the UAS approaches and departs from the static jammer location. In a more realistic scenario, this profile can only be roughly observed because of unknown antenna gain variations. This rough profile is exploited in this implementation to estimate the jamming location and evaluate jamming localization accuracy. This section describes the non-linear received power measurement model, its linearization, and its incorporation in a jammer localization algorithm.

3.1 Received Power Measurement Model

Uncalibrated received power measurements, including those given by the LoRa device's received signal strength indicator (RSSI) which serve as surrogate RFI, can be modeled using the Friis power transmission formula (Wang et al., 2012). In units of decibels of milli-Watts (dBm), this formula can be expressed as (Seidel & Rappaport, 1992)

$$P_{RX} = P_{TX} + G_{TX} + G_{RX} + 10\log_{10}\left(\frac{\lambda^2}{(4\pi)^2 d^n}\right) + v_P \tag{1}$$

where

- P_{RX} is the received power measurement in dBm,
- P_{TX} is the unknown jammer transmitted power in dBm,
- G_{TX} is the unknown transmit antenna gain in the direction of the receiver, which is unitless and often specified in dBi, i.e., as a multiplying factor in log-scale relative to an isotropic antenna,
- G_{RX} is the receiver antenna gain in the direction of the transmitter, in dBi, which may not be calibrated,
- λ is the emitted signal wavelength, in unit of length, which is roughly known when targeting a jamming signal (e.g., centered at GPS L1),
- d is the emitter-to-receiver distance in unit of length,
- n is the signal path loss coefficient, also referred to as environmental factors' coefficient,
- v_P is the received power measurement error in dBm.

Based on offline analysis of nominal received power measurements obtained both at GPS L1 using a USRP and at 868MHz considering a LoRa receiver's RSSI, we assume that v_P is normally distributed with zero mean and variance σ_P^2. We use the notation: $v_P \sim N(0,\ \sigma_P^2)$.

A modified version of Equation (1) is used to capture the facts that: (i) we are not able to distinguish unknown quantities, (ii) we assume uncalibrated received power measurements scaled by an unknown constant quantity, and (iii) some terms other than d will vary during UAS fly-by. The modified version of Equation (1) is given by

$$P_{RX} = -10n\log_{10}(d) + P_E + \xi_E + v_P \quad \text{with} \quad P_E + \xi_E = P_{TX} + G_{TX} + G_{RX} + 20\log_{10}\left(\frac{\lambda}{4\pi}\right) \tag{2}$$

where

- P_E is a constant term that accounts for the constant components of $P_{TX} + G_{TX} + G_{RX} + 20\log_{10}(\lambda/4\pi)$, and for possible scaling constants,
- ξ_E is a time-varying term that accounts for changes in $P_{TX} + G_{TX} + G_{RX}$ which are expected because PPD antennas (e.g., dipole antennas) are anisotropic and cause received power variations as the line-of-sight to the UAS-carried receiver changes during fly-by.

In this phase of the research, a reasonable compromise between model fidelity and practicality is to assume that ξ_E is a time-correlated random variable that can be modeled as a first order Gauss Markov process (FOGMP) such that: $\xi_E \sim N(0,\ \sigma_E^2)$ with a time constant τ_E that will be determined using experimental data. Modeling time-correlation is reasonable in the sense that variations are caused by changes in emitter-to-receiver line-of-sight, which vary over time. It is practical because FOGMPs are easily incorporated in sequential estimators such as Kalman filters by state augmentation, or in batch estimators as will be shown below.

We can express the distance d as a function of the three-dimensional jammer position coordinate vector $\mathbf{x}_J$ (unknown parameter of interest) and the known UAS position vector $\mathbf{p}_{UAS}$, both set in local East-North-Up (ENU) navigation frame. We will account for uncertainty on $\mathbf{p}_{UAS}$ in Sections 3.2. The emitter-to-receiver distance d is given by:

$$d = \sqrt{(p_E - x_E)^2 + (p_N - x_N)^2 + (p_U - x_U)^2} \tag{3}$$

where $$\mathbf{x}_J = \begin{bmatrix} x_E & x_N & x_U \end{bmatrix}^T \quad \text{and} \quad \mathbf{p}_{UAS} = \begin{bmatrix} p_E & p_N & p_U \end{bmatrix}^T \tag{4}$$

We use the vector norm notation $$d = \left\| \mathbf{p}_{UAS} - \mathbf{x}_J \right\| \tag{5}$$

Thus, the non-linear received power measurement equation can be expressed as

$$P_{RX} = h(\mathbf{x}) + \xi_E + v_P \tag{6}$$

where $$h(\mathbf{x}) = -10n\log_{10}(d) + P_E \quad \text{and} \quad \mathbf{x} = \begin{bmatrix} \mathbf{x}_J^T & P_E & n \end{bmatrix}^T \tag{7}$$

Vector **x** is the vector of unknown state parameters to be estimated.

3.2 Linearized Measurement Equations

Using a first order Taylor series approximation to linearize $h(\mathbf{x})$ about an initial guess $\bar{\mathbf{x}}$ of the state vector **x**, Equation (6) becomes

$$P_{RX} \approx h(\bar{\mathbf{x}}) + \mathbf{h}^T (\mathbf{x} - \bar{\mathbf{x}}) + \xi_E + v_P \tag{8}$$

where $$\bar{\mathbf{x}} = \begin{bmatrix} \bar{\mathbf{x}}_J^T & \bar{P}_E & \bar{n} \end{bmatrix}^T \tag{9}$$

The initial guess $\bar{\mathbf{x}}_J$ can be computed by the ground monitor and only needs to provide enough accuracy to deploy the UAS toward the affected region. Nominal values on $\bar{P}_E$ and $\bar{n}$ are given in Section 5 and are sufficient for the algorithm to quickly converge. $\bar{P}_E$ can also be estimated at initialization using Equation (2) given $\bar{n}$, $\bar{\mathbf{x}}_J$, and an initial measurement P_{RX} . The 1×5 observation vector $\mathbf{h}^T$ is expressed as

$$\mathbf{h}^T \triangleq \left. \frac{\partial h(\mathbf{x})}{\partial \mathbf{x}} \right|_{\bar{\mathbf{x}}} = \left. \begin{bmatrix} \dfrac{\partial h(\mathbf{x})}{\partial \mathbf{x}_J} & \dfrac{\partial h(\mathbf{x})}{\partial P_E} & \dfrac{\partial h(\mathbf{x})}{\partial n} \end{bmatrix} \right|_{\bar{\mathbf{x}}} = \begin{bmatrix} \dfrac{10\bar{n}}{\ln(10)\bar{d}} \mathbf{e}^T & 1 & -10\log_{10} \bar{d} \end{bmatrix} \tag{10}$$

where $$\bar{d} = \left\| \mathbf{p}_{UAS} - \bar{\mathbf{x}}_J \right\| \quad \text{and} \quad \mathbf{e}^T \equiv \frac{(\mathbf{p}_{UAS} - \bar{\mathbf{x}}_J)^T}{\left\| \mathbf{p}_{UAS} - \bar{\mathbf{x}}_J \right\|} = \frac{(\mathbf{p}_{UAS} - \bar{\mathbf{x}}_J)^T}{\bar{d}} \tag{11}$$

and $\ln(\cdot)$ is the natural logarithm function. We can express $\bar{d}$ as $\bar{d} = \mathbf{e}^T(\mathbf{p}_{UAS} - \bar{\mathbf{x}}_J)$.

The error in the estimate $\hat{\mathbf{p}}_{UAS}$ of the UAS position vector $\mathbf{p}_{UAS}$ is defined as

$$\delta\mathbf{p}_{UAS} \equiv \hat{\mathbf{p}}_{UAS} - \mathbf{p}_{UAS} \tag{12}$$

The main impact of $\delta\mathbf{p}_{UAS}$ in Equation (8) is on $h(\bar{\mathbf{x}})$, which can be expressed as

$$
\begin{aligned}
h(\bar{\mathbf{x}}) &\equiv -10\bar{n}\log_{10}\left[\mathbf{e}^T(\mathbf{p}_{UAS}-\bar{\mathbf{x}}_J)\right]+\bar{P}_E \\
&= -10\bar{n}\log_{10}\left[\mathbf{e}^T(\hat{\mathbf{p}}_{UAS}+\delta\mathbf{p}_{UAS}-\bar{\mathbf{x}}_J)\right]+\bar{P}_E \\
&= -10\bar{n}\log_{10}\left[\mathbf{e}^T(\hat{\mathbf{p}}_{UAS}-\bar{\mathbf{x}}_J)\left(1+\frac{\mathbf{e}^T\delta\mathbf{p}_{UAS}}{\mathbf{e}^T(\hat{\mathbf{p}}_{UAS}-\bar{\mathbf{x}}_J)}\right)\right]+\bar{P}_E \\
&= -10\bar{n}\log_{10}\left[\mathbf{e}^T(\hat{\mathbf{p}}_{UAS}-\bar{\mathbf{x}}_J)\right]+\bar{P}_E+v_{UAS}
\end{aligned}
\tag{13}
$$

where

$$
v_{UAS} \equiv -10\bar{n}\log_{10}\left[1+\frac{\mathbf{e}^T\delta\mathbf{p}_{UAS}}{\mathbf{e}^T(\hat{\mathbf{p}}_{UAS}-\bar{\mathbf{x}}_J)}\right]. \tag{14}
$$

For small values of the UAS positioning error $\delta\mathbf{p}_{UAS}$, Equation (14) becomes

$$
v_{UAS} \overset{\delta\mathbf{p}_{UAS}\approx 0}{\approx} \frac{10n}{\ln(10)\left\|\hat{\mathbf{p}}_{UAS}-\bar{\mathbf{x}}_J\right\|}\mathbf{e}^T\delta\mathbf{p}_{UAS} \tag{15}
$$

The random variable $\delta\mathbf{p}_{UAS}$ in Equation (15) is assumed to be obtained using Real Time Kinematic (RTK) GNSS and can be modeled as a zero mean normally distributed random vector, such that v_{UAS} is be modeled as

$$
v_{UAS} \sim N(0,\ \sigma_{UAS}^2) \quad \text{with} \quad \sigma_{UAS}^2 \equiv E\left\{v_{UAS}^2\right\} = \frac{100n^2}{[\ln(10)]^2\left\|\hat{\mathbf{p}}_{UAS}-\bar{\mathbf{x}}_J\right\|^2}\mathbf{e}^T\mathbf{P}_{UAS}\mathbf{e} \tag{16}
$$

where $E\{\ \}$ is the expected value operator and $\mathbf{P}_{UAS}$ is the 3×3 UAS positioning error covariance matrix.

Substituting Equation (13) into (8) and rearranging to group all known terms on the left hand side, we obtain the following scalar linearized measurement equation:

$$
z = \mathbf{h}^T\mathbf{x}+v \tag{17}
$$

where

$$
z \equiv P_{RX}+10\bar{n}\log_{10}\left[\mathbf{e}^T(\hat{\mathbf{p}}_{UAS}-\bar{\mathbf{x}}_J)\right]-\bar{P}_E+\mathbf{h}^T\bar{\mathbf{x}} \quad \text{and} \quad v \equiv -v_{UAS}+\xi_E+v_P \tag{18}
$$

3.3 Non-Linear Least Squares Estimator

Power measurements z_k are collected at time step k at time t_k, for $k=1,\ldots,q$, i.e., over the duration of one or more UAS fly-bys to estimate the constant state parameter vector $\mathbf{x}$. In this early implementation, we post-process data in a batch non-linear least-squares (NLS) estimator using a Newton-Raphson method with a priori information. Future implementations will explore sliding window mechanisms and extended Kalman filters. The linearized batch measurement equation is written as:

$$
\mathbf{z} = \mathbf{H}\mathbf{x}+\mathbf{v} \tag{19}
$$

where

$$
\mathbf{z} \equiv \begin{bmatrix} z_1 \\ \vdots \\ z_q \end{bmatrix}, \quad \mathbf{H} \equiv \begin{bmatrix} \mathbf{h}_1^T \\ \vdots \\ \mathbf{h}_q^T \end{bmatrix}, \quad \text{and} \quad \mathbf{v} \equiv \begin{bmatrix} \xi_{E,1}-v_{UAS,1}+v_{P,1} \\ \vdots \\ \xi_{E,q}-v_{UAS,q}+v_{P,q} \end{bmatrix}.
$$

Over an interval t_i to t_j, the discrete-time FOGMP can be expressed as

$$
\xi_j = \alpha_{i,j}\xi_i + v_{\xi,i} \quad \text{where} \quad \alpha_{i,j} \equiv e^{-|t_i-t_j|/\tau_E}
$$

The FOGMP driving noise $v_{\xi,i}$ is zero mean white Gaussian noise. The measurement error model assumptions in Sections 3.1 and 3.2 are captured in the following q×1 measurement error vector model:

$$\mathbf{v} \sim N(\mathbf{0},\ \mathbf{V}) \tag{20}$$

with
$$\mathbf{V} = \begin{bmatrix} \sigma_E^2 + \sigma_{UAS,1}^2 + \sigma_P^2 & \sigma_E^2 \alpha_{1,2} & & \sigma_E^2 \alpha_{1,q} \\ \sigma_E^2 \alpha_{1,2} & \sigma_E^2 + \sigma_{UAS,2}^2 + \sigma_P^2 & & \\ & & \ddots & \vdots \\ \sigma_E^2 \alpha_{1,q} & & \cdots & \sigma_E^2 + \sigma_{UAS,q}^2 + \sigma_P^2 \end{bmatrix}.$$

Matrix **V** is a Toeplitz matrix, which makes it easy to construct in practice. The time correlation due to UAS positioning errors is small relative to that of ξ_E and is neglected in this implementation.

Section 3.2 describes the initial guess $\bar{\mathbf{x}}$ ($\bar{\mathbf{x}} = [\bar{\mathbf{x}}_J^T \quad \bar{P}_E \quad \bar{n}]^T$) on the state vector. We assume the following prior knowledge covariance matrix:

$$\bar{\mathbf{P}} = \begin{bmatrix} \bar{\mathbf{P}}_J & \mathbf{0} & \mathbf{0} \\ \mathbf{0} & \sigma_E^2 & 0 \\ \mathbf{0} & 0 & \sigma_n^2 \end{bmatrix} \tag{21}$$

We derive a state estimate vector $\hat{\mathbf{x}}$ and its covariance matrix $\hat{\mathbf{P}}$ (and, over multiple iterations, we refine the linearization point $\mathbf{x}_*$ (initially, $\mathbf{x}_* = \bar{\mathbf{x}}$) and the resulting coefficients of $\mathbf{H} = \mathbf{H}|_{\mathbf{x}_*} = \mathbf{H}_*$) using the following equations:

$$\hat{\mathbf{x}} = \bar{\mathbf{x}} + \bar{\mathbf{P}}\mathbf{H}_*^T(\mathbf{V} + \mathbf{H}_*\bar{\mathbf{P}}\mathbf{H}_*^T)^{-1}(\mathbf{z} - \mathbf{H}_*\bar{\mathbf{x}}) \tag{22}$$

$$\hat{\mathbf{P}} = \bar{\mathbf{P}} - \bar{\mathbf{P}}\mathbf{H}_*^T(\mathbf{V} + \mathbf{H}_*\bar{\mathbf{P}}\mathbf{H}_*^T)^{-1}\mathbf{H}_*\bar{\mathbf{P}} \tag{23}$$

We monitor the following convergence metric:

$$(\mathbf{x}_* - \hat{\mathbf{x}})^T \hat{\mathbf{P}}^{-1}(\mathbf{x}_* - \hat{\mathbf{x}}) \tag{24}$$

which decreases exponentially in all experimental tests described below.

4 EXPERIMENT SETUP

4.1 Test Bed

Figure 3 shows the test bed, which consists of a quad-rotor UAS equipped with an RF receiver, a surrogate jammer providing RSSI measurements, a lightweight onboard computer to collect and time-stamp position and power measurements, and a ground station for UAS telemetry and RTK corrections.

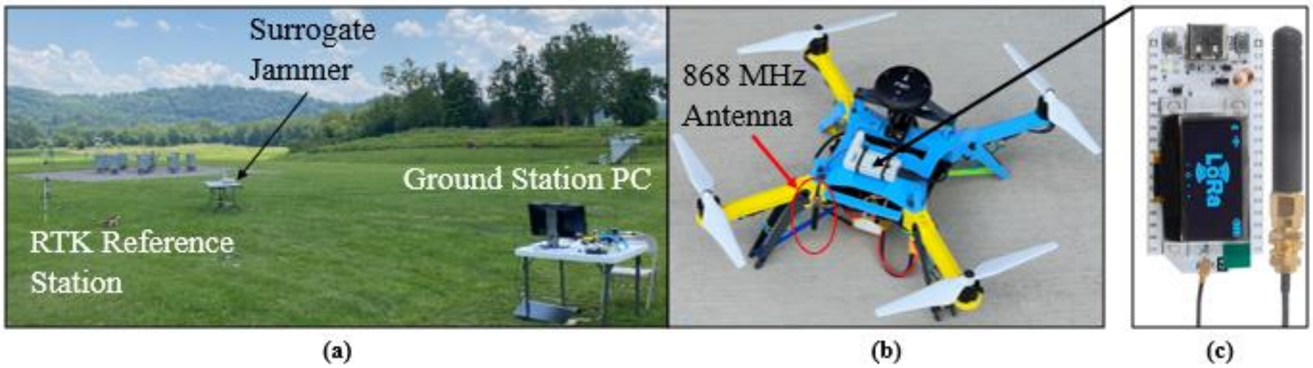

FIGURE 3 Hardware setup at the Virginia Tech Kentland Experimental Aerial Systems lab (KEAS): **(a)** Control, RTK reference, and surrogate jammer stations **(b)** RTK-configured quad-rotor UAS with onboard PC **(c)** Heltec LoRa ESP32 development board with antenna.

Figure 4 gives an overview of the experimental hardware components. The UAS uses a flight controller with integrated IMU and RTK-GPS receiver to fly pre-determined trajectories and estimate UAS locations with sub-meter-level accuracy. The surrogate jammer and monitor are ESP32 LoRa development boards, one mounted to a tripod acting as a jammer while the other is onboard the UAS. These transceivers exchange data packets using a LoRa protocol over 868 MHz frequency from which RSSI is extracted at the UAS. A Raspberry-Pi 4 is mounted on the UAS to collect and time-stamp RSSI and vehicle pose using the Robotic Operating System (ROS).

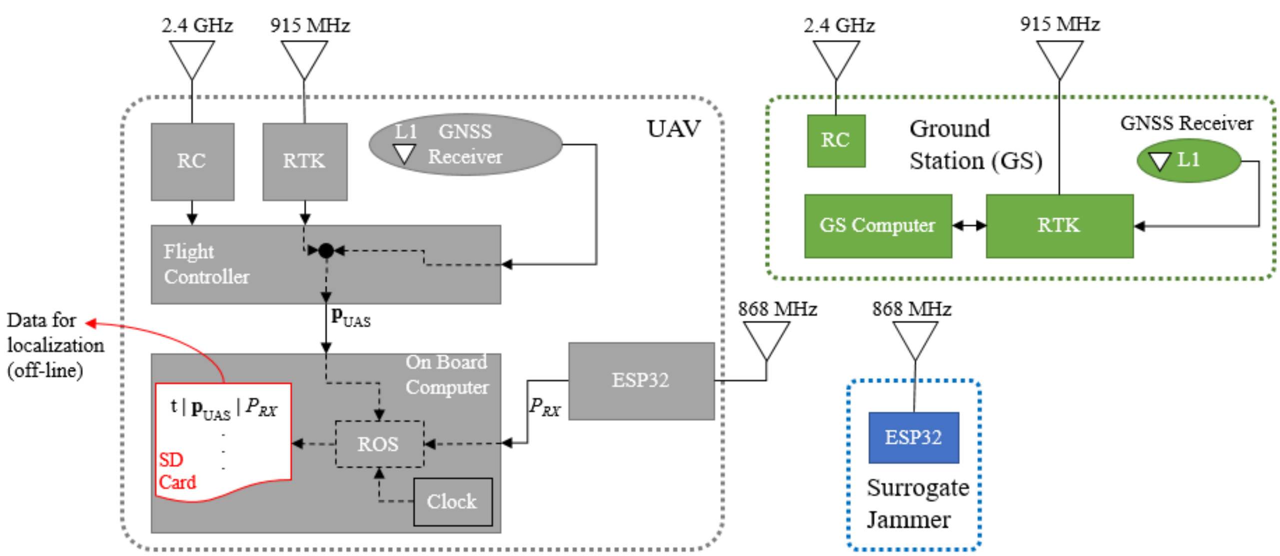

FIGURE 4 Experimental hardware and communication architecture.

The hardware in Figure 4 was selected for its low SWAP-C characteristics and commercial availability. Future implementations where jammer localization is performed in flight to localize actual GNSS jammers will require more capable onboard computer and a software-defined receiver. Table A in Appendix provides additional information on testbed hardware.

4.2 Experiment Scenarios

Three flight scenarios were planned as shown in Figure 5. The first two tests were conducted with the UAS serving as a mobile sensor payload that was held 1.5-meter-high and walked in a desired trajectory near the surrogate jammer. The third experiment was performed with the UAS flying a pre-planned trajectory roughly 5 meters above the RF source. These trajectories are intended to provide LOS measurements oriented in both the East and North directions. While the RF sensors, onboard computer, and ground station hardware were identical for each experiment, the UAV and associated flight controllers used in the hand-held and flying experiments were different models. The experiments were performed in the VT KEAS test area without any occlusions between transceivers. The data was post-processed in MATLAB.

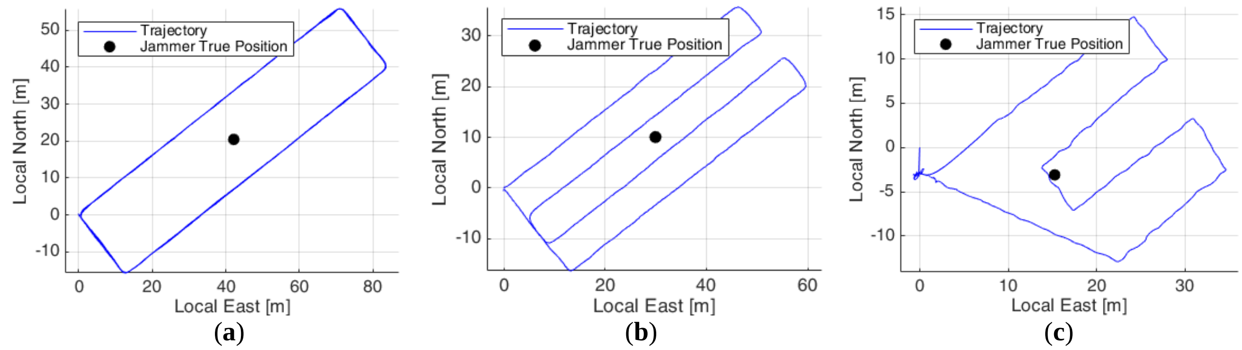

FIGURE 5 Maps of three planned flight trajectories: (**a**) (carried) Circling, (**b**) (carried) Lawnmower, and (**c**) Flying

5 EXPERIMENTAL RESULTS

Table 2 lists initial state and measurement error model parameter values used for all three experiments. The initial location assumed on the location of the jammer differs for each experiment, but is within 5 meters in all three dimensions of the true location for the given experiment.

TABLE 2

Localization parameters and initial conditions

Parameter	Initial Value	Units
$\bar{\mathbf{x}}_J^T$	$\bar{\mathbf{x}}_{J,true}^T + [5 \quad 5 \quad 5]$	m
$\bar{P}_E$	-85	dBm
$\bar{n}$	2.1	Unit-less
$\sigma_{\bar{P}_E}$	20	dBm
σ_J	10	m
σ_{P_E}	10	dBm
σ_P	15	dBm
σ_n	0.5	Unit-less
σ_{UAS}	0.09	m
τ_E	30	s

5.1 Data Set 1: Carried Payload – Circling Trajectory

Figure 6 shows the algorithm's performance in modeling distance and received power (RSSI) compared to true and measured. Figure 6(a) shows the measured receiver power, P_{RX}, as a function of true distance to the jammer: $d_{true} = \left\| \mathbf{p}_{UAS} - \mathbf{x}_{J,true} \right\|$. The estimated RSSI model is received power estimated over time as: $\hat{P}_{RX} = \hat{P}_E - 10\hat{n}\log_{10}\left(\hat{d}\right)$, where $\hat{d} = \left\| \mathbf{p}_{UAS} - \hat{\mathbf{x}}_J \right\|$. Figure 6(b) compares d_{true} to $\hat{d}$ over time, while figure 6(c) does the same for P_{RX} and $\hat{P}_{RX}$. The light blue shaded region is the estimated RSSI uncertainty (1σ).

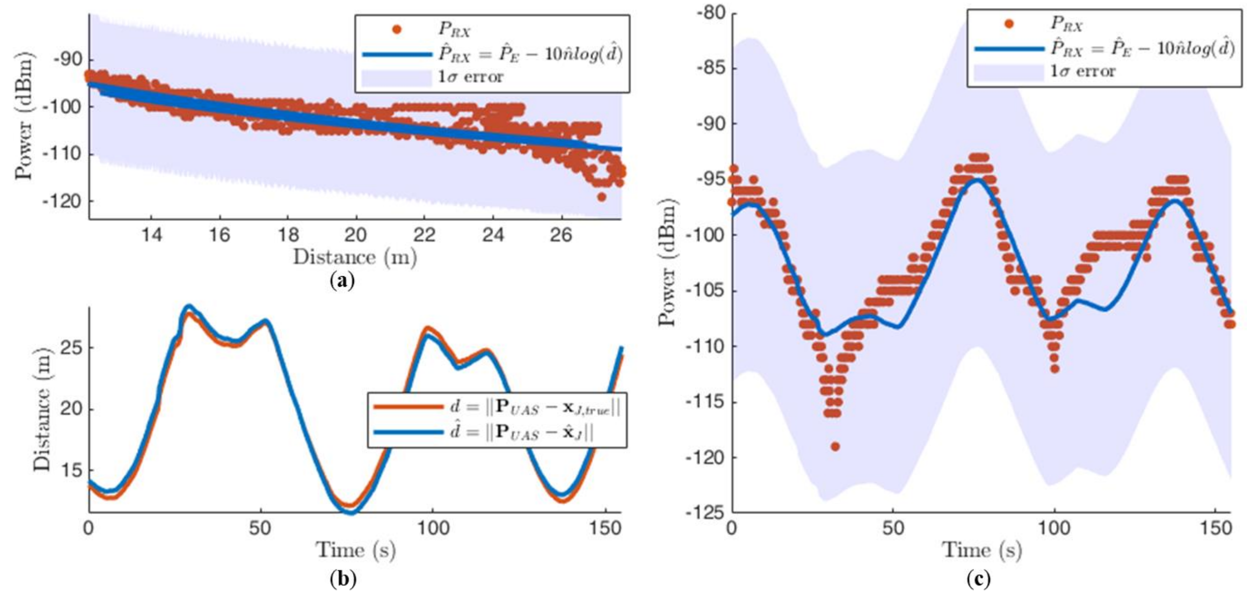

FIGURE 6 Model vs measured values for the carried circling experiment conducted on 7/11/2023, where: (**a**) received power (RSSI) vs distance between recievers, (**b**) distance between recievers over time, and (**c**) RSSI over time.

Both estimated jammer-UAS distance and RSSI model track with the true and measured values closeley. Figure 7 shows the full trajectory with a final three-dimensional (3D) jammer location estimate error of 0.8m, which is within the predicted jammer position estimate covariance ellipse. By circling the source, adequate measurements were taken in both the North and East directions, leading to a near circular 1σ estimate error covariance ellipse.

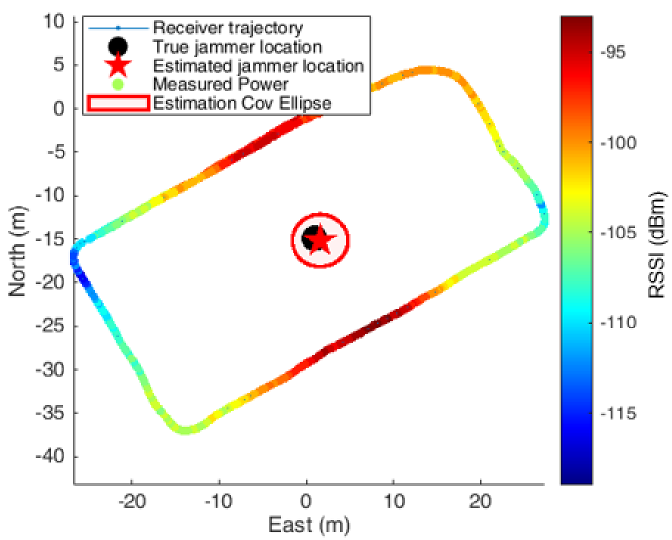

FIGURE 7 UAS trajectory, measured RSSI, and true and estimated jammer location for the circling carried experiment conducted at KEAS on 7/11/2023.

5.2 Data Set 2: Carried Payload – Lawnmower Trajectory

Figures 8 and 9 show the same performance metrics as above for the carried lawnmower trajectory experiment conducted on 9/11/2023. Figure 9 shows the semi-minor axis of the position estimate error covariance ellipse aligned in the northeast direction, which is expected from greater motion and more measurements taken in the northeast direction for this trajectory. The final 3D jammer position estimate is 1.3m to the northeast of the true location of the jammer.

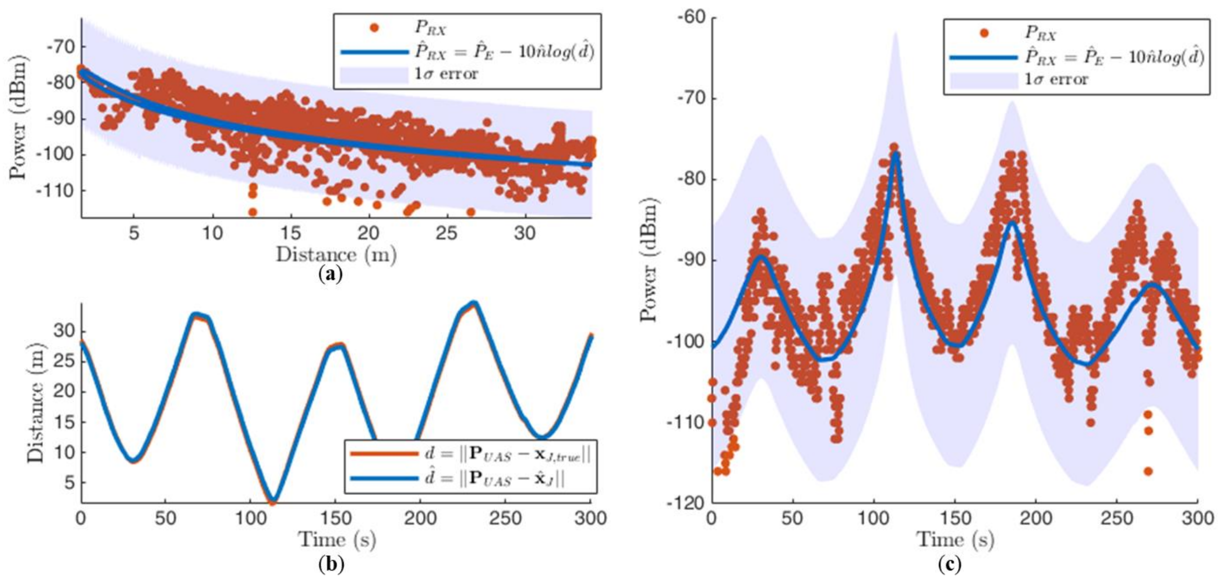

FIGURE 8 Model vs measured values for the carried UAS in a lawnmower pattern experiment conducted on 9/11/2023, where: (**a**) received power (RSSI) vs distance between recievers, (**b**) distance between recievers over time, and (**c**) RSSI over time.

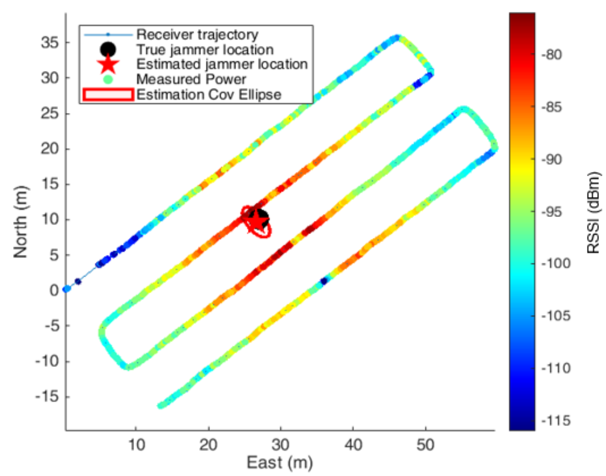

FIGURE 9 Experimental RF source localization result for the UAS flight experiment on 9/11/2023.

5.3 Data Set 3: Flying Payload

Figures 10 and 11 show the performance of the localizer during the UAS flight experiment conducted on 12/24/2023. Figure 10(b) and (c) show that the model fits the sparse data well. Figure 10(a) shows the estimated RSSI (blue) as a function of UAS-jammer distance. In Figure 10 (b), $\hat{d}$ does not match d_{true} as closely as in previous data sets. Sparse data collection in the first leg of the experiment were due to occlusions caused by the UAS battery. This can be seen when comparing Figure 5(c) to the northwest section of Figure 11.

The RSSI heat map in Figure 11 does not match expectations nearly as well as in the carried experiments. All three northeast-aligned legs of the trajectory show power measurements that are inconsistent with the concept that received power increases as the UAS approaches the source. Yellow and green markers at the northeast-most sections of the trajectory are separated from the jammer's true location by weak power readings (blue). This indicates the presence of an occlusion (battery, or part of the UAS). Other contributing factors include antenna gain pattern effects not observed in the previous experiments where the two transceiver antennas were nearly coplanar. In particular, power drops can be explained by the UAS vertical dipole antenna flying at a higher altitude near the zenith of emitter's vertical dipole antenna. The two antenna's combined effect may explain the gap in power measurements between 160s and 200s in Figure 10(c). Future work will further analyze the impacts of antenna gain patterns. In Figure 11, the jammer's 3D position estimate was 3.8 meters off of the true position.

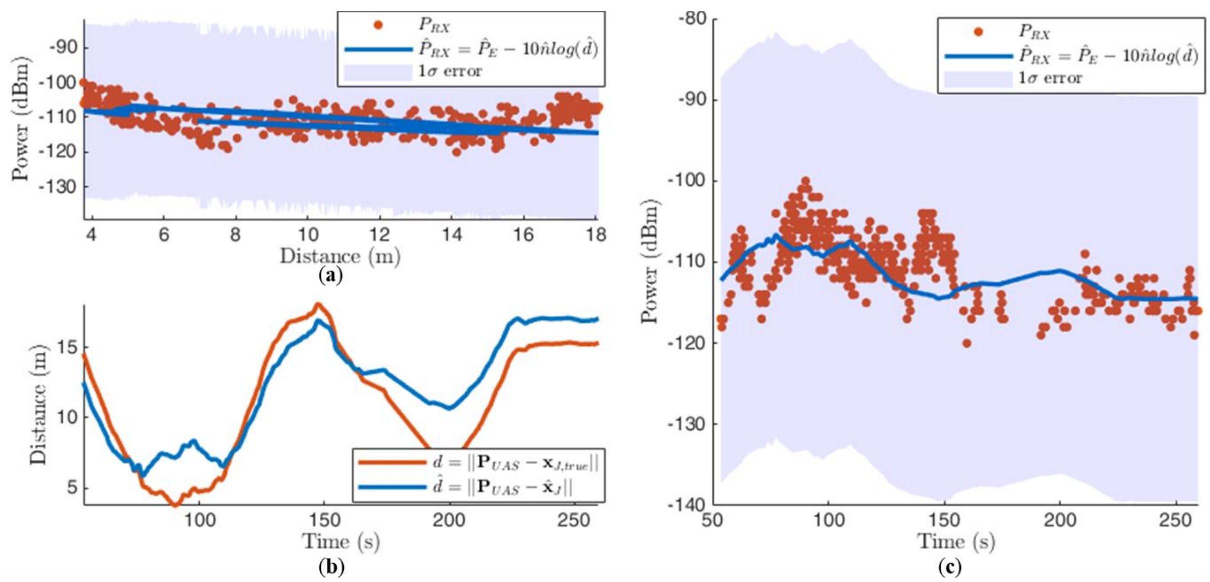

FIGURE 10 Model vs measured values for the flying experiment conducted on 12/21/2023, where: (**a**) received power (RSSI) vs distance between recievers, (**b**) distance between recievers over time, and (**c**) RSSI over time.

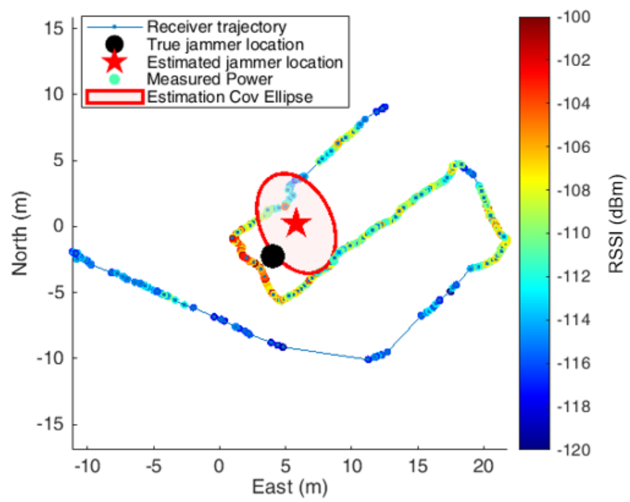

FIGURE 11 UAS trajectory, measured RSSI, and true and estimated jammer location for the flying experiment on 12/21/2024.

6 CONCLUSION

We developed and tested a method for localizing a GNSS jammer using power measurements collected on a UAS flying a pre-planned trajectory. A linearized power measurement equation based on Friis' power transmission law was implemented in a NLS sequential batch estimation algorithm. Three experiments were conducted with different trajectories using an 868 MHz LoRa WiFi as a surrogate jammer. Meter-level RF source localization errors in all directions were achieved across experiments when coarse prior knowledge on jammer location is provided and variations due to unknown RF transmission parameters are accounted for using a first order Gauss Markov process. Future work includes further sensitivity analysis of the impacts on localization accuracy of received power model fidelity and prior knowledge of jammer location.

ACKNOWLEDGMENT
This paper is based upon research sponsored by the Center for Autonomous Air Mobility & Sensing (CAAMS) supported by the National Science Foundation (NSF)'s Industry-University Cooperative Research Centers (IUCRC). Any opinions, findings, or recommendations expressed in this publication are those of the Author(s) and do not necessarily reflect the view of the sponsors. The authors also thank Zakia Ahmed for flight test support.

REFERENCES
Bauernfeind, R., & Eissfeller, B. (2014). Software-defined radio based Roadside Jammer Detector: Architecture and Results. *2014 IEEE/ION Position, Location and Navigation Symposium - PLANS 2014*. https://doi.org/10.1109/plans.2014.6851504

Bhamidipati, S., & Gao, G. X. (2018). Simultaneous localization of multiple jammers and receivers using probability hypothesis density. *2018 IEEE/ION Position, Location and Navigation Symposium (PLANS)*. https://doi.org/10.1109/plans.2018.8373472

Bhamidipati, S., & Gao, G. X. (2019). Locating multiple GPS jammers using networked uavs. *IEEE Internet of Things Journal*, *6*(2), 1816–1828. https://doi.org/10.1109/jiot.2019.2896262

Borio, D., & Gioia, C. (2015). Real-time jamming detection using the sum-of-squares paradigm. *2015 International Conference on Location and GNSS (ICL-GNSS)*. https://doi.org/10.1109/icl-gnss.2015.7217161

Clements, Z., Ellis, P., Psiaki, M., & Humphreys, T. E. (2022). Geolocation of terrestrial GNSS spoofing signals from low Earth orbit. *ION GNSS+, The International Technical Meeting of the Satellite Division of The Institute of Navigation*. https://doi.org/10.33012/2022.18444

Goward, D. (2019, December 17). Chinese GPS spoofing circles could hide Iran oil shipments - GPS world. GPS World - The Business and Technology of Global Navigation and Positioning. https://www.gpsworld.com/chinese-gps-spoofing-circles-could-hide-iran-oil-shipments/

Goward, D. (2021, April 21). *Russia ramps up GPS jamming along with troops at Ukraine border - GPS world*. GPS World - The Business and Technology of Global Navigation and Positioning. https://www.gpsworld.com/russia-ramps-up-gps-jamming-along-with-troops-at-ukraine-border/

Gromov, K., Akos, D., Pullen, S., Enge, P., & Parkinson, B., "GIDL: Generalized Interference Detection and Localization System," Proceedings of the 13th International Technical Meeting of the Satellite Division of The Institute of Navigation (ION GPS 2000), Salt Lake City, UT, September 2000, pp. 447-457.

Güzey, N. (2022). RF source localization using multiple uavs through a novel geometrical RSSI approach. *Drones*, *6*(12), 417. https://doi.org/10.3390/drones6120417

Harris, M. (2020, June 17). *Ghost ships, crop circles, and Soft Gold: A GPS mystery in Shanghai*. MIT Technology Review. https://www.technologyreview.com/2019/11/15/131940/ghost-ships-crop-circles-and-soft-gold-a-gps-mystery-in-shanghai/

Hasanzade, M., Herekoglu, O., Yeniceri, R., Koyuncu, E., & Inalhan, G. (2018). RF source localization using unmanned aerial vehicle with Particle Filter. *2018 9th International Conference on Mechanical and Aerospace Engineering (ICMAE)*. https://doi.org/10.1109/icmae.2018.8467555

Jada, S., Bowman, J., Psiaki, M., Fan, C., & Joerger, M. (2022). Time-frequency analysis of GNSS jamming events detected on U.S. highways. *ION GNSS+, The International Technical Meeting of the Satellite Division of The Institute of Navigation*. https://doi.org/10.33012/2022.18528

Jada, S., Bowman, J., Psiaki, M., Langel, S., & Joerger, M. (2023). Identifying car key fobs as a cause of interference at GNSS frequencies. *Proceedings of the 36th International Technical Meeting of the Satellite Division of The Institute of Navigation (ION GNSS+ 2023)*. https://doi.org/10.33012/2023.19376

Jada, S., Psiaki, M., Landerkin, S., Langel, S., Scholz, A., & Joerger, M. (2021). Evaluation of PNT situational awareness algorithms and methods. *Proceedings of the 34th International Technical Meeting of the Satellite Division of The Institute of Navigation (ION GNSS+ 2021)*. https://doi.org/10.33012/2021.17935

Joerger, M., Jada, S., & Fan, C. (2023, October 6). *The unsolved mystery of the 2022 Texas interference*. Inside GNSS - Global Navigation Satellite Systems Engineering, Policy, and Design. https://insidegnss.com/the-unsolved-mystery-of-the-2022-texas-interference/#:~:text=The%20October%202022%20Texas%20jamming,airspace%20above%20Dallas%20Fort%20Worth.

Jones, M. (2020, May 12). *Spoofing in the Black Sea: What really happened? - GPS world*. GPS World - The Business and Technology of Global Navigation and Positioning. https://www.gpsworld.com/spoofing-in-the-black-sea-what-really-happened/#:~:text=Firstly%2C%20it%20didn't%20happen,a%20large%2Dscale%20spoofing%20attack.

Kwon, H., & Guvenc, I. (2023). RF signal source search and localization using an autonomous UAV with predefined waypoints. *2023 IEEE 97th Vehicular Technology Conference (VTC2023-Spring)*. https://doi.org/10.1109/vtc2023-spring57618.2023.10200783

Liu, B., Zhu, X., Jiang, Y., Wei, Z., & Huang, Y. (2019). UAV and piecewise convex approximation assisted localization with unknown path loss exponents. *IEEE Transactions on Vehicular Technology*, *68*(12), 12396–12400. https://doi.org/10.1109/tvt.2019.2946142

Liu, Z., Lo, S., & Walter, T., "Characterization of ADS-B Performance under GNSS Interference," Proceedings of the 33rd International Technical Meeting of the Satellite Division of The Institute of Navigation (ION GNSS+ 2020), September 2020, pp. 3581-3591. https://doi.org/10.33012/2020.17675

Marcos, E. P., Konovaltsev, A., Caizzone, S., Cuntz, M., Yinusa, K., Elmarissi, W., & Meurer, M. (2018). Interference and spoofing detection for GNSS maritime applications using direction of arrival and conformal Antenna Array. *Proceedings of the 31st International Technical Meeting of The Satellite Division of the Institute of Navigation (ION GNSS+ 2018)*. https://doi.org/10.33012/2018.15901

Murfin, T. (2023, October 18). *GPS jamming in Israel - GPS World*. GPS World - The Business and Technology of Global Navigation and Positioning. https://www.gpsworld.com/gps-jamming-in-israel/

Murrian, M. J., Narula, L., Iannucci, P. A., Budzien, S., O'Hanlon, B. W., Psiaki, M. L., & Humphreys, T. E. (2021). First results from three years of GNSS interference monitoring from low Earth orbit. *NAVIGATION*, *68*(4), 673–685. https://doi.org/10.1002/navi.449

Perkins, A., Dressel, L., Lo, S., Reid, T., Gunning, K., & Enge, P. (2016). Demonstration of UAV based GPS jammer localization during a live interference exercise. *Proceedings of the 29th International Technical Meeting of The Satellite Division of the Institute of Navigation (ION GNSS+ 2016)*. https://doi.org/10.33012/2016.14661

Pullen, S., & Gao, G. X. (2018, April 22). *GNSS jamming in the name of privacy*. Inside GNSS - Global Navigation Satellite Systems Engineering, Policy, and Design. https://insidegnss.com/gnss-jamming-in-the-name-of-privacy/

Seidel, S. Y., & Rappaport, T. S. (1992). 914 mhz path loss prediction models for indoor wireless communications in multifloored buildings. *IEEE Transactions on Antennas and Propagation*, *40*(2), 207–217. https://doi.org/10.1109/8.127405

Šture, F., Morong, T., Kovar, P., & Puricer, P. (2019). High performance SDR for monitoring system for GNSS jamming localization. *2019 International Conference on Wireless Networks and Mobile Communications (WINCOM)*. https://doi.org/10.1109/wincom47513.2019.8942521

Wang, G., Chen, H., Li, Y., & Jin, M. (2012). On received-signal-strength based localization with unknown transmit power and path loss exponent. *IEEE Wireless Communications Letters*, *1*(5), 536–539. https://doi.org/10.1109/wcl.2012.072012.120428

Wu, G. (2019). UAV-based interference source localization: A multimodal Q-learning approach. *IEEE Access*, *7*, 137982–137991. https://doi.org/10.1109/access.2019.2942330

APPENDIX

TABLE A
Hardware Description and Test Parameter Settings

Hardware	Flight Controller	GNSS RTK Base Station	GNSS RTK Receiver	ESP 32 (Jam / Mon)	On board PC	RC	Telemetry Radio
Description	Pixhawk 6X mini	H-RTK F9P Base	H-RTK F9P Rover lite	Heltec WiFi LoRa 32(V3)	Raspberry-Pi 4 Model B	FrSKY Taranis X9D Plus	SiK Telemetry Radio V3
Part Number	20175	12022	12017	N/A	N/A	N/A	17013
OS	N/A	N/A	N/A	Arduino	Ubuntu 18.04	N/A	N/A
Software	PX4 1.14.0	U-center	U-center	C++ Script	ROS Melodic	N/A	SIK firmware
Processor	STM32H753	UBLOX F9P module	UBLOX F9P module	ESP32-S3FN8	ARM Cortex-A72	N/A	N/A
RF Frequency	N/A	L1: 1.57 MHz	L1: 1.57 MHz	LoRa: 868 MHz	N/A	2.4 GHz	915 MHz